Highly active PdCeO$_x$ composite catalysts for low-temperature CO oxidation, prepared by plasma-arc synthesis

R.V. Gulyaev[a], E.M. Slavinskaya[a], S.A. Novopashin[b], D.V. Smovzh[b], A.V. Zaikovskii[b], D.Yu. Osadchii[d], O.A. Bulavchenko[a], S.V. Korenev[c,d], A.I. Boronin[a,d,*]

[a] Boreskov Institute of Catalysis SB RAS, Novosibirsk, Russian Federation
[b] Kutateladze Institute of Thermophysics SB RAS, Novosibirsk, Russian Federation
[c] Nikolaev Institute of Inorganic Chemistry SB RAS, Novosibirsk, Russian Federation
[d] Novosibirsk State University, Novosibirsk, Russian Federation

ABSTRACT

The plasma-arc method was adapted for the synthesis of composite palladium–ceria catalysts, which were utilized for the low-temperature oxidation of carbon monoxide. The Pd/CeO$_2$ catalysts were synthesized in two steps: step 1 – direct synthesis of palladium–cerium–carbon composite PdCeC in the plasma-arc chamber, and step 2 – calcination of the composite with carbon burnout in air at 600, 700, and 800 °C. Catalytic testing using temperature-programmed reaction demonstrated the high efficiency of the synthesized catalysts during the oxidation of carbon monoxide and their ability to oxidize CO at temperatures as low as room temperature. In comparison with a catalyst that had similar morphology and palladium content but was prepared by coprecipitation, the synthesized catalyst showed that the calculated TOF value for the composite catalyst was two–three times higher than that of the catalyst prepared by chemical methods.

A variety of physical methods (HRTEM, XRD, XPS, Raman spectroscopy and others) were used to examine the microstructure, composition and electronic state of the composite components in detail after the high-temperature calcination stage of catalyst synthesis. It was shown that high catalytic activity was provided by the formation of a high-defect fluorite structure of PdCeO$_x$ solid solution and highly dispersed PdO$_x$ nanoparticles. The XPS data suggest that carbon nanostructures mixed with palladium and cerium in the initial PdCeC composite prevent sintering during high-temperature calcination and play a key role in the formation of a high-defect solid solution of palladium in the CeO$_2$ structure, which has a high concentration of Ce^{3+} and oxygen vacancies.

© 2013 Elsevier B.V. All rights reserved.

1. Introduction

Pd/CeO$_2$ catalysts, which contain palladium and cerium dioxide, are some of the most promising catalysts used for the oxidation of hydrocarbons [1–6] and harmful gases, especially carbon monoxide [7–9]. Currently, the catalytic oxidation of carbon monoxide, which yields CO$_2$, is a very convenient and efficient method for processing automotive exhausts and industrial off-gases, thus protecting the atmosphere and environment. The challenge in designing catalytic technologies for carbon monoxide removal is the promotion of oxidation at ambient or even lower temperatures. Catalysts that can perform low-temperature oxidation with carbon monoxide (LTO CO) substantially extend the application scope of pollution scrubbing technologies, such as the cleaning of enclosed spaces and the neutralization of vehicle exhaust.

Recently, various LTO CO catalysts have been synthesized and studied [10]. Each type of catalyst has both advantages and drawbacks; catalysts applicable to every case are not known to exist. Palladium–cerium oxide catalysts are notable for their high activity, successful oxidation at low temperatures (∼0 °C), and high stability over a wide range of temperatures (up to 800 °C and above). Sources in the literature attribute these properties to the strong chemical interactions between palladium and cerium oxide [11,12]. The deposition of palladium stimulates the mobility of the oxygen in the CeO$_2$ lattice and also retains the oxygen storage capacity of CeO$_2$ [13,14]; in the process, palladium is finely dispersed and predominantly exists in ionic states [11,15].

The unique performance of these catalysts is determined not only by the active component (palladium) but also by the combination of palladium with cerium oxide. For example, Pd/Al$_2$O$_3$ catalysts, which consist of Pd and PdO nanoparticles supported on alumina, are active toward the oxidation of CO only at temperatures

* Corresponding author at: Boreskov Institute of Catalysis SB RAS, Novosibirsk, Russian Federation. Tel.: +7 3833269631; fax: +7 3833308056.
E-mail addresses: boronin@catalysis.ru, boronin@catalysis.nsk.su (A.I. Boronin).

above 150 °C [16]; however, Pd/CeO$_2$ catalysts are able to oxidize CO even at ambient and lower temperatures [6–9].

Currently, most researchers have concluded that the active sites in palladium-containing catalysts for CO LTO are not metallic and/or oxide nanoparticles, unlike the more conventional Pd/Al$_2$O$_3$ catalyst. In the literature, the most popular view is that, on the surface of these catalysts, palladium forms single ionic sites as components of Pd$_x$Ce$_{1-x}$O$_2$ solid solutions [5,11,15,17–19]. However, the structure of these solid solutions and the electronic states of palladium are still not fully elucidated [20–25]; the various research teams involved in these studies disagree on the exact structure of the Pd$_x$Ce$_{1-x}$O$_2$ solid solution and on the oxidation state of palladium. This disagreement results from the scarcity of high-precision experimental data concerning the properties of Pd/CeO$_2$ catalysts and from a dearth of new approaches to the synthesis of palladium–cerium oxide systems, especially those that promote maximum interaction between palladium and cerium oxide. Currently, the prevailing chemical methods for the preparation of Pd/CeO$_2$ include impregnation [3,15,26–28], precipitation [4,29], microemulsification [18,30], and solution combustion [5,8,11,17]. However, the development and application of advanced techniques that expose a substance to harsh physical action to obtain Pd/CeO$_2$ catalysts are also important. These techniques are intended to produce structures with unusual morphology, which would display different properties than more conventionally synthesized Pd/CeO$_2$ catalysts, and to reveal the details of the Pd$_x$Ce$_{1-x}$O$_2$ interaction phase; alternative techniques include microwave discharge [9], aerosol synthesis [31], hydrothermal synthesis [32,33] and plasma-arc processing [34–37].

In this work, we suggested and implemented an advanced method that uses plasma-arc discharge for the synthesis of a nanoscale palladium–cerium oxide catalyst. The application of an electric arc in the synthesis of nanomaterials is based on the pioneering work by Kratschmer and co-authors [38], which was devoted to fullerene synthesis. The proposed technology was subsequently employed to synthesize carbon nanotubes [39] and, later, metal–carbon nanoparticles, which required the use of an electric arc in a buffer of inert gas at a low pressures (1–500 Torr) [40,41]. Effective anode erosion occurs in the direct current arc, leading to the formation of monatomic components of the anode in the high-temperature region.

In this work, plasma-arc technology was used to synthesize composite oxide nanoparticles. The process was implemented in two steps: synthesis of metal nanoparticles on a carbon matrix and calcination of the synthesized material in an oxygen-containing atmosphere. This sequence enabled us to eliminate the carbon matrix and to synthesize oxide nanoparticles composed of a PdO–CeO$_2$ mixed oxide.

This study was designed to adapt techniques of plasma-arc discharge to the synthesis of a palladium–cerium oxide system and to investigate this oxide system's physicochemical and catalytic properties during the oxidation of carbon monoxide. The results of this study demonstrate that the plasma-arc method facilitates the synthesis of palladium–cerium oxide systems that are active in LTO CO and comparable in activity with the best Pd/CeO$_2$ catalysts generated by traditional chemical methods.

2. Experimental

2.1. Catalyst preparation

The first step in the catalyst preparation was the synthesis of the PdCeC, or cerium–palladium–carbon, composite. The experiments were carried out in a direct current electric arc, which had a current of 100 A, in a buffer gas (helium) at 25 Torr. The spray electrode

(anode) was a graphite rod 70 mm in length and 7 mm in diameter. A hole was drilled in the center of the electrode for the insertion of a cerium rod 2.8 mm in diameter; palladium foil was mounted to achieve a Pd/Ce weight ratio of 3%. Monatomic spray products diffused in the buffer gas from the hot zone of the arc, which resulted in the cooling and heterogeneous condensation of the spray products. The composite material was precipitated on a cooled shield located 5 cm from the arc discharge area. The synthesized material consisted of metal nanoparticles on a carbon matrix. For the second step, the synthesized PdCeC composite was calcined in air at 600, 700 and 800 °C to produce a nanosized Pd$_x$Ce$_{1-x}$O$_2$ composite. The resulting material was tested for catalytic activity in the LTO CO reaction and characterized by a set of physical methods.

The catalysts obtained by arc synthesis are denoted 3PdCeC-BR, 3PdCeC-600-BR, 3PdCeC-700-BR and 3PdCeC-800-BR; the first number indicates the palladium content and the second number indicates the calcination temperature. The BR index denotes a freshly prepared catalyst sample, whereas the samples exposed to the reaction medium are marked AR.

The 3.8PdCe-P-700 catalyst was prepared by coprecipitation from Pd(NO$_3$)$_2$ and Ce(NO$_3$)$_3$ aqueous solutions with NaOH at pH = 6, followed by calcination of the precipitate at 700 °C in air for 4 h. Index P stands for precipitation, which was used for comparison purposes. The other indices are similar to those for the catalysts synthesized by the plasma-arc method.

2.2. Investigation of the catalytic properties

The catalytic properties of the synthesized catalysts were examined in the oxidation of CO with oxygen using a temperature-programmed reaction (TPR-CO + O$_2$). The experiments were automated and utilized a flow reactor with in-line mass-spectrometric analysis of the gas mixture. The initial sample, which had particle sizes from 0.5 to 0.25 mm, was placed into the stainless steel reactor. Capacity of the reactor was 0.25 cm^3. Details of the reactor design were considered in [42]. At the initial temperature of −10 °C, a reaction mixture containing 0.2 vol.% CO, 1.0 vol.% O$_2$, 0.5 vol.% Ne, and helium, which made up the balance, was fed at a rate of 1 L/min. The space velocity was 240,000 h^{-1}. The sample was heated in the reactor to 450 °C at a rate of 10 °C/min.

2.3. Investigation by physical methods

X-ray diffraction analysis (XRD) was carried out on a Bruker D8 Advance diffractometer, which was equipped with a Lynxeye (1D) linear detector, over the angular range of 10–75° at 2θ = 0.05° with a storage time of 1 s for each point. Monochromatic CuK$_\alpha$ radiation (λ = 1.5418 Å) was employed in these experiments. The average size of the coherent scattering cross-sections was estimated by the Scherrer equation [43].

High-resolution transmission electron microscopy (HRTEM) micrographs were obtained using a JEM-2010 electron microscope (JEOL, Japan) with a lattice-fringe resolution of 0.14 nm and an accelerating voltage of 200 kV. The high-resolution images of the periodic structures were analyzed by the Fourier method. Local energy-dispersive X-ray analysis (EDXA) was carried out using an EDX spectrometer (EDAX Co.), which was fitted with a Si (Li) detector, at a resolution of 130 eV. The samples for the HRTEM study were prepared on a perforated carbon film mounted on a copper grid.

Raman spectra for the Pd/CeO$_2$ samples calcined in air were taken on a Spex Triplemate instrument (Princeton Instruments, USA) at a wavelength of λ = 488 nm. Spectra for the initial PdCeC composites were not obtained because the samples combusted under laser radiation.

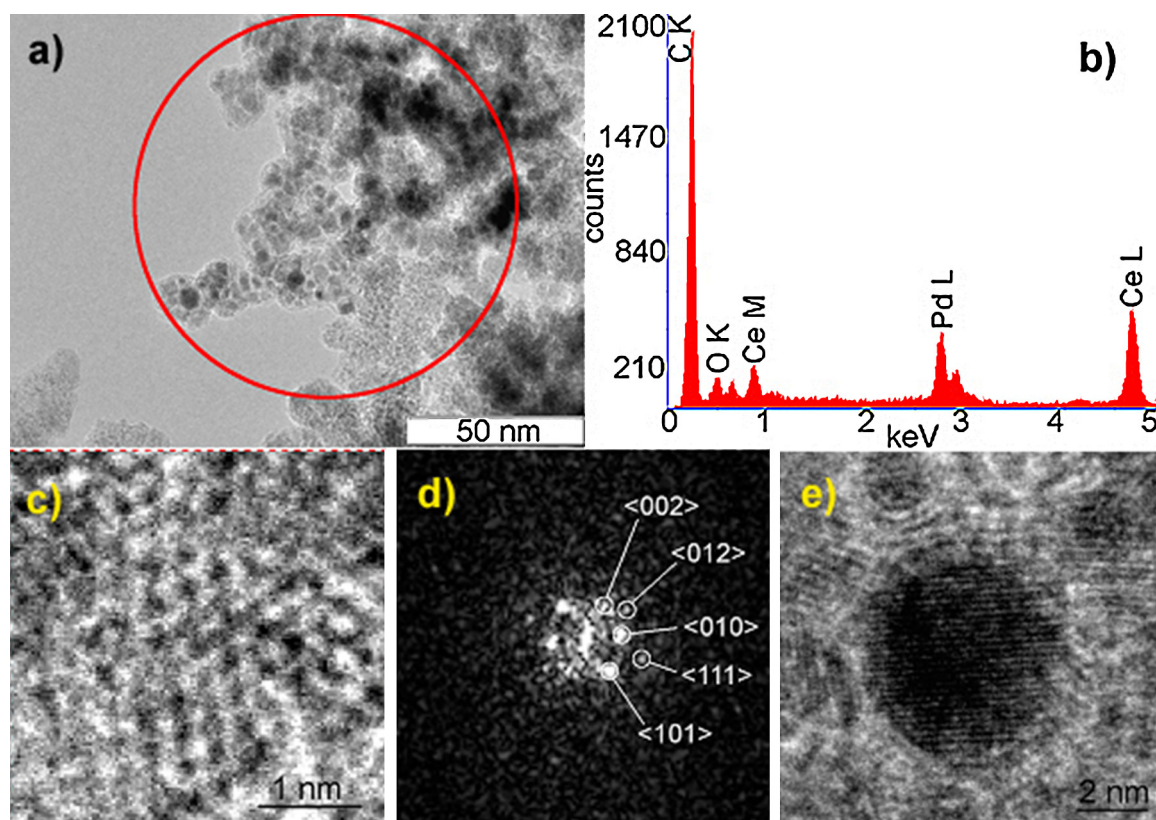*Thermogravimetric experiments* were performed on a DTG60H instrument (Shimadzu Scientific Instruments).

Fig. 1. (a) TEM micrograph of the synthesized 3PdCeC-BR material, (b) EDX spectrum obtained from the selected region, (c) Ce_2O_3 crystal lattice and (d) its Fourier image, (e) Pd nanoparticle with the resolved crystal structure.

The surface areas of the samples were measured according to the BET method.

Photoelectron spectroscopy of the samples was carried out using a ES300 photoelectron spectrometer (KRATOS Analytical, UK). The spectra were recorded using polychromatic MgK_α radiation ($h\nu = 1253.6\,eV$) as a low power X-ray source ($13\,kV \times 6\,mA$) to prevent a photoinduced reduction of the sample surface. For XPS analysis, the samples were powdered and fixed on a holder with double-sided carbon tape. Spectra of the main photoelectron lines of individual elements were recorded with a binding energy step of 0.1 eV at fixed pass energy of 25 eV for the electronic analyzer. The spectrometer was calibrated against the $Au4f_{7/2}$ and $Cu2p_{3/2}$ lines of gold and copper, and their binding energies were taken to be 84.0 and 932.7 eV, respectively [44]. The spectra were calibrated against the U‴ component of the Ce3d spectra of the Ce^{4+} ion using the reference value $E_b = 916.7\,eV$ [44]. Experimental curves were processed with XPS-Calc software, which has been tested with some earlier systems [15,16,42,45,46]. The decomposition of the spectra curves into individual components was performed using a combination of Gaussian and Lorentzian functions after background subtraction by the Shirley method.

3. Results and discussion

3.1. Thermogravimetric analysis

According to thermogravimetric analysis in air, a sharp release of heat occurs at a temperature near 300 °C, which leads to an approximately 25% weight loss. The further elevation of temperature causes a gradual weight loss until these changes virtually cease at 600–700 °C. In the range of 800–900 °C, the sample retains nearly 40% of its initial weight. These values agree with the theoretical

weight loss caused by the oxidation of carbon, its subsequent removal to the gas phase, and the weight gain caused by the oxidation of cerium to CeO_2. Based on the TGA measurements, we have chosen 600, 700 and 800 °C as calcination temperatures for the synthesized samples. The TGA diagram for the composite is displayed in the Supplementary information section.

3.2. Morphology and phase composition

Surface area measurements for the initial composite material 3%PdCeC and its samples calcined in air at 600, 700 and 800 °C gave values of 157, 94, 66 and 57 m^2/g, respectively. Note that the surface areas of the synthesized Pd/CeO_2 catalysts are quite high and comparable to those of the catalysts prepared by traditional chemical techniques. Additionally, increasing the calcination temperature from 600 to 800 °C does not lead to catastrophic sintering of the composite, which is corroborated by the surface area decrease (a factor of ~1.5). This indicates high thermal stability of the synthesized composite. According to our earlier study of pure CeO_2 samples, calcination at 800 °C leads to sintering of CeO_2 nanoparticles into crystallites of size 200–500 nm; in the process, the specific surface area decreases from 87 (for cerium oxide calcined at 450 °C) to 3 m^2/g at a calcination temperature of 800 °C [15].

Electron microscopy (TEM) and energy dispersive X-ray analysis (EDX) of the synthesized PdCeC material indicated that it consisted mainly of amorphous carbon particles 5–50 nm in size with inclusions of crystal nanoparticles 2–10 nm in size (Fig. 1a) that contained cerium and palladium (Fig. 1b). The TEM data clearly demonstrated that the developed surface area of the PdCeC composite is determined by the formation of carbon particles.

High-resolution transmission electron microscopy of the initial composite revealed the presence of crystal structures corresponding to cerium α-oxide (Ce_2O_3) (Fig. 1c). The nanocrystals were
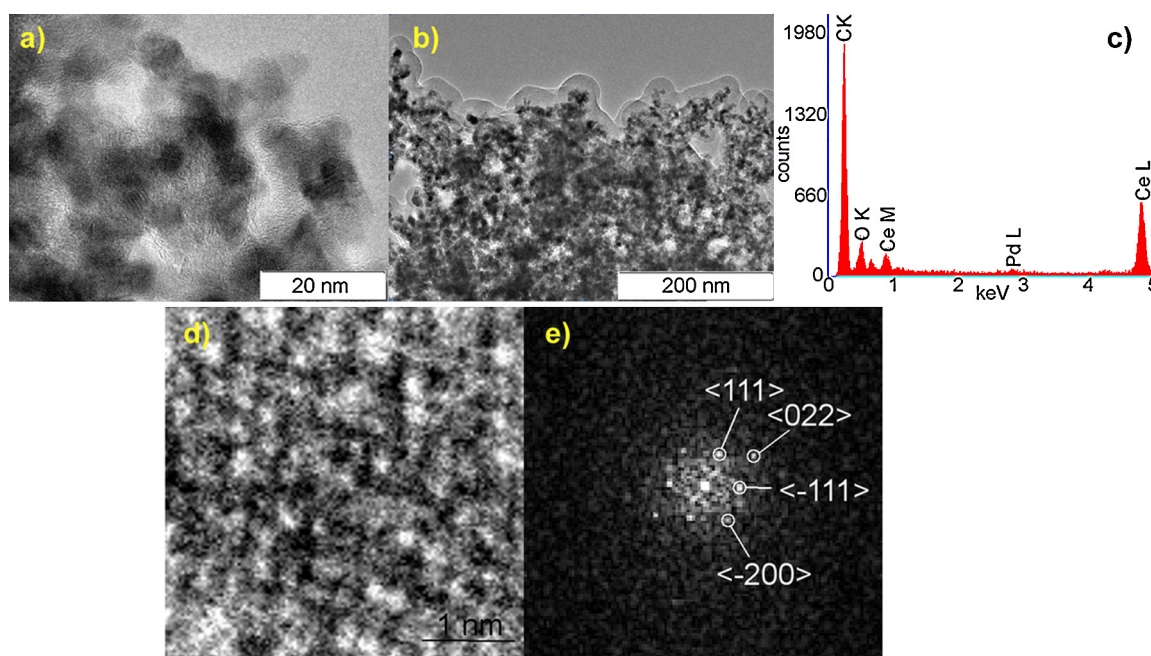
Fig. 2. (a and b) TEM micrographs of the 3PdCeC-600-BR sample, (c) EDX elemental analysis, (d) micrograph of the CeO₂ nanocrystal lattice and (e) its Fourier image for the 3PdCeC-600-BR sample.

identified by constructing the Fourier images of the crystal lattices (Fig. 1d). The reflections on the Fourier image, displayed in Fig. 1d, correspond to the interplanar distances of 0.319, 0.2307, 0.3316, 0.1965 and 0.2879 nm. Taking into account these distances and the arrangement of the reflections, it can be suggested that Fig. 1d shows a Ce_2O_3 nanocrystal with a trigonal lattice, which has the following reference data for interplanar distances: 0.303 nm ||0 0 2||, 0.22502 nm ||0 1 2||, 0.33602 nm ||1 0 0||, 0.18476 nm ||1 1 1|| and 0.29387 nm ||0 1 1||. A set of equivalent planes, ||1 0 0||, includes the family of parallel planes (0 1 0), and the 0 1 1 set includes the (1 0 1) family; therefore, the positions of the reflections on the Fourier image displayed in Fig. 1d agree with the reference data for Ce_2O_3. All of the images with resolved crystal lattices were identified in a similar manner. Taking into account the EDX spectra, we concluded that the crystal structure of the material comprises mainly Ce_2O_3 nanocrystals, a small amount of metallic Pd nanocrystals (Fig. 1e), and carbon with signs of graphitization.

According to the TEM micrographs (Fig. 2a) of the material calcined at 600 °C, the material consists of 5–10 nm nanoparticles. Some sections of the material are covered with amorphous carbon (Fig. 2b). The presence of carbon in the sample is confirmed by EDX analysis (Fig. 2c).

High resolution TEM showed that the nanoparticles are CeO_2 particles with a cubic crystal lattice. Fig. 2d and e shows the micrograph of the CeO_2 crystal lattice and its Fourier image. The arrangement of the reflections on the Fourier image and the interplanar distances corresponding to these reflections (0.3183, 0.1904, 0.3125 and 0.2707 nm) allowed us to determine that the crystal lattice corresponds to CeO_2 with the reference interplanar distances of 0.3124 nm ||1 1 1||, 0.19131 nm ||2 0 2||, and 0.27055 nm ||2 0 0||.

Fig. 3 (curve 1) shows the experimental X-ray pattern of the initial sample. In the diffraction pattern of the sample, there are two narrow peaks that correspond to the graphite structure [PDF #41-1187] and indicate the graphitization of the carbon matrix. No peaks attributable to cerium, palladium, or their derivative compounds were observed in the spectra. In our opinion, there are two reasons for the absence of reflections from Ce_2O_3 phase in the XRD pattern of the initial composite. First, the symmetry group of

α-Ce_2O_3 phase is not the highest one, which implies the presence of many diffraction peaks with a low intensity. Second, according to HRTEM data, the size of identified Ce_2O_3 particles rarely exceeds 3–4 nm, which indicates a very high dispersion of this phase in the initial composite. In its turn, this should lead to a strong diffusion of the diffraction peaks for this phase. Taking into account the first and second reasons, the absence of pronounced peaks of the Ce_2O_3 phase in the diffraction pattern of initial composite is quite expectable.

X-ray diffraction analysis validated the TEM data. After calcination at 600 °C (Fig. 3, curve 2), a narrow graphite peak remains and reflections from CeO_2 appear in the X-ray pattern [PDF #43-1002]. After further calcination, the graphite peak disappears and,
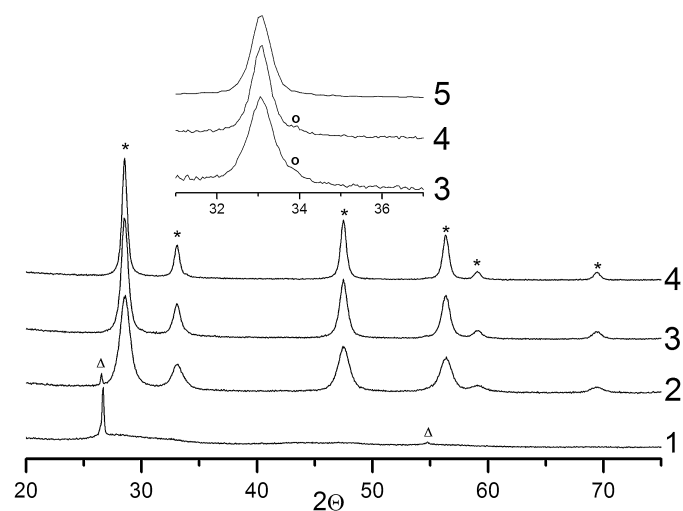

Fig. 3. X-ray patterns of the initial sample 3PdCeC-BR (1), 3PdCeC-600-BR (2), 3PdCeC-700-BR (3), and 3PdCeC-800-BR (4). The insert displays a fragment of the X-ray patterns for the 3PdCeC-700-BR (3) and 3PdCeC-800-BR (4) samples and 3.8Pd/CeO2-P-700 reference sample (5). Triangles indicate the reflections of graphite, the asterisks mark CeO_2, and circles denote PdO.

at 700 °C, a small shoulder appears at $2\theta = 33.9°$, which can be attributed to the crystallization of PdO (Fig. 3, curve 3). In the sample calcined at 800 °C, a peak appears that corresponds to the most intense 1 0 1 reflection of PdO [PDF #41-1107] (Fig. 3, curve 4). The mean crystalline sizes of the CeO_2 particles for the samples calcined at 600, 700 and 800 °C are 90, 145 and 210 Å, respectively, because the ceria particles sinter when the calcination temperature increases. One can see that an increase in the calcination temperature of cerium oxide leads to sintering of the CeO_2 phase and formation of larger particles. This was expected to decrease lattice parameter of the composite to a value typical of pure ceria (5.411 Å). However, in the experiments, an increase in the size of particles was accompanied by a minor increase in the lattice parameter from 5.414 to 5.416 Å for the samples calcined at 700 and 800 °C. As was shown by different research groups, incorporation of palladium into the ceria lattice with the formation of $Pd_xCe_{1-x}O_2$ solid solutions at a high palladium concentration increases the lattice parameter, respectively, to 5.413 Å at the $Pd_{0.05}Ce_{0.95}O_{1.95}$ stoichiometry, and to 5.416 Å at the $Pd_{0.1}Ce_{0.9}O_{1.9}$ stoichiometry, whereas at the $Pd_{0.02}Ce_{0.95}O_{1.95}$ stoichiometry the lattice parameter of such solution does not differ from the corresponding value for pure CeO_2 (5.411 Å) [47]. Another publication of the same research group shows that at the $Pd_{0.01}Ce_{0.99}O_{1.90}$ stoichiometry the lattice parameter decreases from 5.4113 Å for pure CeO_2 to 5.4107 Å and then to 5.4101 Å at the $Pd_{0.03}Ce_{0.97}O_{1.87}$ stoichiometry [7]. In [48], the lattice parameter of the $Pd_{0.01}Ce_{0.99}O_{2-\delta}$ solid solution was 5.417 Å. The authors of [49] observed an increase in the lattice parameter of 1.5%Pd/CeO_2 sample to 5.418 Å. In [50] the lattice parameter of a solid solution increased linearly with increasing palladium fraction, up to 5.418 Å at the $Pd_{0.1}Ce_{0.9}O_{2-\delta}$ stoichiometry. A similar linear growth of the lattice parameter with increasing palladium fraction in $Pd_xCe_{1-x}O_{2-\delta}$ solid solutions was observed in [18]. The lattice parameter reached 5.455 Å at the $Pd_{0.2}Ce_{0.8}O_{2-\delta}$ stoichiometry. Note that at the $Pd_{0.035}Ce_{0.965}O_{2-\delta}$ stoichiometry the lattice parameter was 5.416 Å according to the authors. If the entire palladium introduced into the sample forms a solid solution, such solution should have the $Pd_{0.05}Ce_{0.95}O_{2-\delta}$ stoichiometry.

In addition, the diffraction pattern of the reference sample 3.8Pd/CeO2-P-700 shows only the reflections of ceria phase with the corresponding size of particles, 170 Å, whereas the reflections typical for palladium oxide are absent (see the insert on Fig. 3). The lattice parameter of ceria phase in this catalyst is also increased, reaching 5.417 Å. It means that in this case, the dissolution of palladium oxide in ceria with the formation of the $Pd_xCe_{1-x}O_2$ solid solution is also most likely to occur.

Overall, our data agree with the data reported by other researchers; it can be stated that the crystal lattice of the studied composites is distorted and differs from the structure of perfect CeO_2 fluorite. The most reasonable hypothesis is dissolution of palladium in the ceria structure to form the $Pd_xCe_{1-x}O_2$ solid solution.

Therefore, the XRD data show that increasing the calcination temperature of the samples leads to both the sintering of ceria and the dissolution of some of the palladium in the ceria lattice. Residual palladium forms the PdO nanoparticles.

3.3. Catalytic activity

Fig. 4 shows the conversion's temperature dependence during the oxidation of CO. According to this figure, the initial carbon-containing 3PdCeC composite appears to be inactive at temperatures below 220 °C, indicating that it is inactive in the CO LTO region ($T < 150$ °C), and the temperature where 50% conversion (T_{50}) is observed is approximately 260 °C. Repeated cooling and heating of initial composite in the reaction mixture leads to a sharp increase in the catalytic activity; the T_{50} value decreases to 150 °C. This effect may be related to continued carbon elimination during the
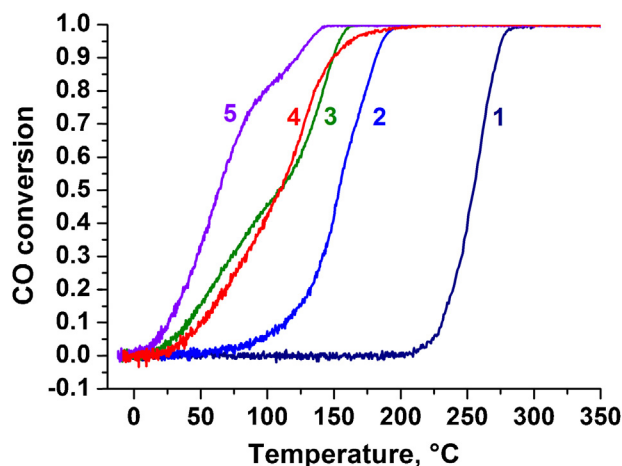

Fig. 4. The CO-O_2 TPR curves for catalysts 3PdCeC (1, 2), 3PdCe-600 (3), 3PdCe-700 (5) and 3PdCe-800 (4) obtained during the first heating to 450 °C (1) and during repeated heating after cooling (2–5).

first heating stage, which results in the formation of active surface components that are accessible to the reaction mixture. Nevertheless, the catalyst remains inactive in the low-temperature region of $T < 100$ °C.

Calcination of the composite in air at 600 °C induces low-temperature activity ($T < 150$ °C), in which T_{10} and T_{50} are equal to 42 and 110 °C, respectively. Raising the calcination temperature to 700 °C produces a further increase in the initial activity ($T_{10} = 27$ °C, $T_{50} = 64$ °C), and the catalyst approaches the CO LTO parameters for efficient catalysts that are prepared by conventional impregnation techniques [15,44,46]. A further increase in the calcination temperature decreases the catalytic activity of the sample ($T_{10} = 50$ °C, $T_{50} = 110$ °C). The best catalytic performance is observed for the catalyst calcined at 700 °C.

3.4. Surface composition and state of the elements according to XPS

XPS was used to examine the initial 3PdCeC-BR composite and its samples calcined in air at temperatures of 600, 700 and 800 °C. Taking into account the fact that catalytic testing included the heating in the reaction mixture to 450 °C, the 3PdCeC-AR sample of the initial composite after catalytic testing was also examined by XPS.

3.4.1. Analysis of C1s and Ce3d spectra

A substantial amount of elementary carbon (Fig. 5a, curve 1) forming the carbon matrix is located on the surface of the initial 3PdCeC-BR composite. The position of the main component of the C1s line (284.6 eV) and the presence of components responsible for relaxation $\pi-\pi^*$ transitions (low intensity peaks at 290–292 eV) indicate that the ground state of carbon corresponds to the sp^2 hybrid state [51,52]. Additional peaks with E_b(C1s) = 286.0 eV and 288–289 eV can be attributed to sp^3 structures and carbonates [43], respectively. The occurrence of these additional signals may be related to the presence of the oxygen admixture in the gas discharge chamber during composite synthesis. This oxygen can affect the surface of the carbon nanoparticles, thus forming carbonate structures. Additionally, another explanation that cannot be ruled out is that, after the synthesis of the nanocomposite, a portion of surface carbon atoms can have unsaturated valences and can therefore be highly reactive toward oxygen, which can lead to interactions with oxygen when the sample is taken out of the chamber. However, the concentration of oxidized carbon species is low; these species cannot play an essential role in the formation of the composite
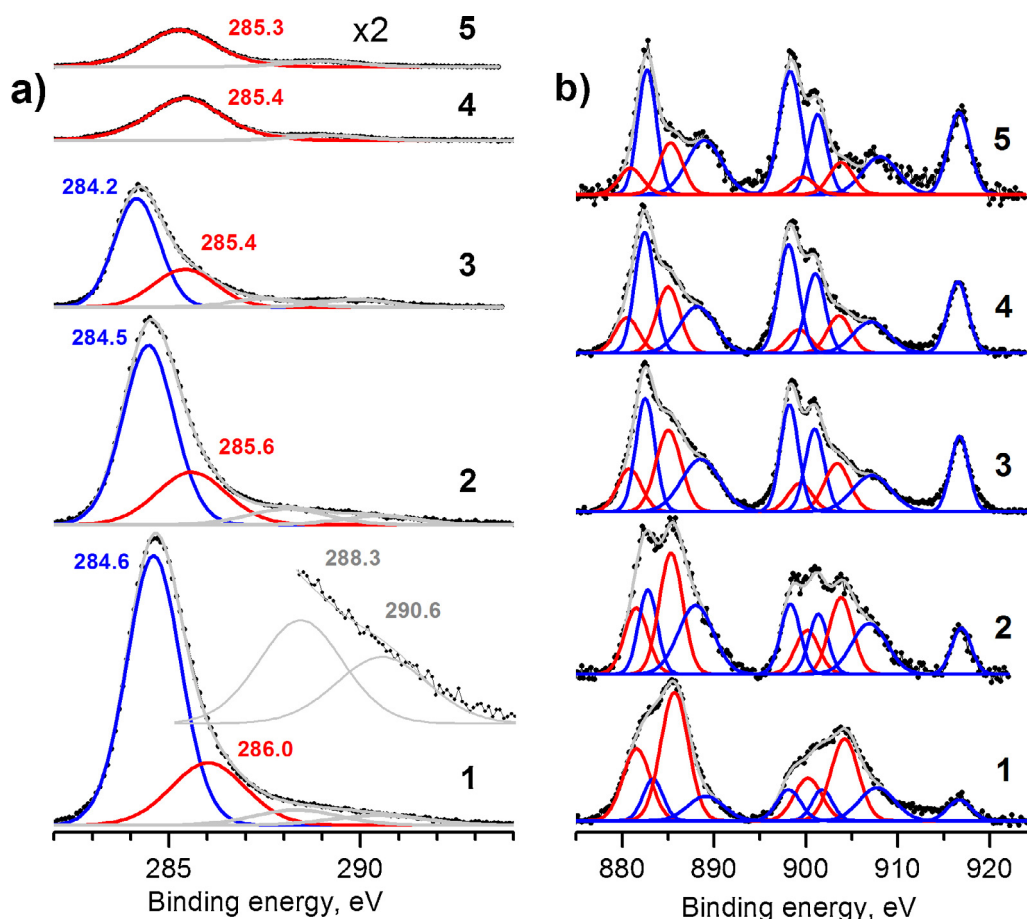
Fig. 5. Normalized spectra of the C1s (a) and Ce3d lines (b) for samples (1) 3PdCeC-BR, (2) 3PdCeC-AR, (3) 3PdCeC-600-BR, (4) 6PdCeC-700-BR, and (5) 6PdCeC-800-BR. The intensity of the C1s spectrum (a, curve 5) is magnified twofold for better visibility. Red components in (b) correspond to the Ce^{3+} ions and blue components denote the Ce^{4+} ions. (For interpretation of the references to color in this figure legend, the reader is referred to the web version of this article.)

properties that are important for catalyst synthesis. Additionally, it should be noted that, in the C1s spectra, there are no features with $E_b(C1s) < 284$ eV, which would indicate the presence of a carbide-like cerium species.

The valent state of cerium (Fig. 5b, curve 1), which was determined by the five-doublet decomposition of the Ce3d line [46], is composed of approximately 70% Ce^{3+} ions. Therefore, the high content of Ce^{3+} ions indicates that the initial composite contains mostly Ce_2O_3 nanoparticles, according to the HRTEM data reported above. The presence of Ce^{4+} ions can be attributed to the partial oxidation of these particles on the surface when the sample is transferred in air prior to XPS analysis.

After catalytic testing, a large amount of carbon is still present in the 3PdCeC-AR sample, although its amount decreases nearly 1.5-fold (Fig. 5a, curve 2); this observation may be related to the partial burnout of the carbon matrix over the course of catalytic testing. The concentration of each carbon species decreases nearly proportionally; however, the peak corresponding to the sp³ component shifts, whereas the position of the peak for the sp² component remains virtually unchanged (Fig. 5a, curve 2). These observations can be explained by the following: size effects on the chemical shift of the C1s line are most pronounced for carbon sp³ structures.

The surface of the support particles is strongly oxidized due to the action of the reaction medium, which is indicated by a decrease in the fraction of Ce^{3+} ions to 50%. Evidently, complete oxidation to CeO_2 does not occur because the fraction of Ce^{3+} ions remains quite high.

Calcination at 600 °C leads to a further decrease in the intensity of the C1s line; this step also produces a minor shift for the sp² component in the C1s spectrum to 284.2 eV, and the sp³ component shifts to 285.4 eV (Fig. 5a). After the further elimination of carbon, the more extended crystallized carbon structures may remain unburnt because their burnout requires higher calcination temperatures. Analysis of the Ce3d spectrum (Fig. 5b, curve 3) indicates that the fraction of Ce^{3+} ions decreases to 32%. According to the HRTEM and XRD data, this decrease is related to the formation of CeO_2 particles with a defect structure containing high concentrations of anion vacancies and Ce^{3+} ions. A large portion of the Ce^{3+} ions in the structure of the CeO_2 particles calcined at 600 °C in air can be attributed to the stabilization of the surface/subsurface defects due to the carbon structures present in this defect lattice of cerium oxide nanoparticles.

An increase in the calcination temperature of the composite to 700 °C leads to a further intense elimination of carbon and concurrent oxidation of the surface. In the C1s spectrum of the 3PdCeC-700-BR sample, a component with a binding energy of 284.2 eV disappears, similar to the shake-up satellites (Fig. 5a, curve 4), indicating a complete combustion of the graphite-like species in the composite. However, the sp³ component, which has a binding energy of 285.4 eV, remains virtually unchanged; these data indicate that this species is much less reactive than the graphite nanoparticles (Table 1).

Calcination of the catalyst at 800 °C does not produce substantial changes to the state of the carbon; its binding energy remains

Table 1
Binding energies of the photoelectron line components of the samples versus calcination temperature.

Sample	Binding energy (eV)				
	$Pd3d_{5/2}$		Ce3d(U‴)	C1s	
3PdCe-BR	336.0	337.7	916.7	284.5	286.0
3PdCe-AR	335.7	338.0	916.7	284.5	285.6
3PdCe-600	336.5	338.0	916.7	284.2	285.4
3PdCe-700	336.3	338.0	916.7	–	285.4
3PdCe-800	336.3	337.9	916.7	–	285.2

equal to 285.3 eV (Fig. 5a, curve 5). However, the amount of carbon decreases nearly twofold (see Table 2), indicating that the process of carbon elimination was not complete. The position of the peak corresponding to this species is E_b(C1s) = 285.4 eV and is quite stable to oxygen during the calcination of the composite; therefore, it seems reasonable to classify this sp^3 species as carbon constituting the clusters incorporated into the cerium oxide structure. This incorporation may be why the cerium oxide lattice is not transformed into the lattice of the highly structured CeO_2 by calcination and also why it contains a considerable amount (28%) of Ce^{3+} ions, as determined from the Ce3d spectrum in Fig. 5b, curve 5 (Table 2).

3.4.2. Analysis of Pd3d spectra

The state of palladium is characterized by the Pd3d line, which has a strongly distorted shape in the case of the initial composite, extended toward higher binding energies (Fig. 6, curve 1). The decomposition of this spectrum reveals three doublets: the main doublet, which has a binding energy of the $Pd3d_{5/2}$ line equal to 336.0 eV and two additional doublets with E_b($Pd3d_{5/2}$) = 338.0 and 340.5 eV (Fig. 6, curve 1). The ground state of palladium with E_b($Pd3d_{5/2}$) = 336.0 eV may correspond to both specific oxidized structures of palladium [53,54] and small (subnanometer) metallic clusters [55,56]. However, taking into account the strong carbonizing nature of the atmosphere used in the synthesis of the initial composite, it seems reasonable to attribute this doublet to a palladium carbide or carbide-like state. This interpretation can be supported by the data recently obtained by synchrotron radiation photoelectron spectroscopy (SRPES) [57], which assigned the PdC_x state with E_b($Pd3d_{5/2}$) = 335.8–336.0 eV.

The peak with E_b($Pd3d_{5/2}$) = 338.0 eV, based on the data from [4,6,7,15,46], can be attributed to the oxidized palladium–cerium structures composing the $Pd_xCe_{1-x}O_2$ solid solution.

The state of palladium with E_b($Pd3d_{5/2}$) = 340.5 eV deserves special attention. This binding energy of the Pd3d level is very high in terms of the chemical shift caused by the initial charge state; it cannot be attributed to even a superoxidized state of palladium (Pd^{4+}). Additionally, the presence of a conductive carbon matrix in this sample implies the absence of differential charging of the surface when recording XPS spectra. The narrowness of the C1s, Ce3d (Fig. 5) and O1s (not shown) spectral lines observed in the experiment for this sample confirms this assumption. Therefore, a component with the binding energy of 340.5 eV can be attributed neither to a charging effect nor to a superoxidized state
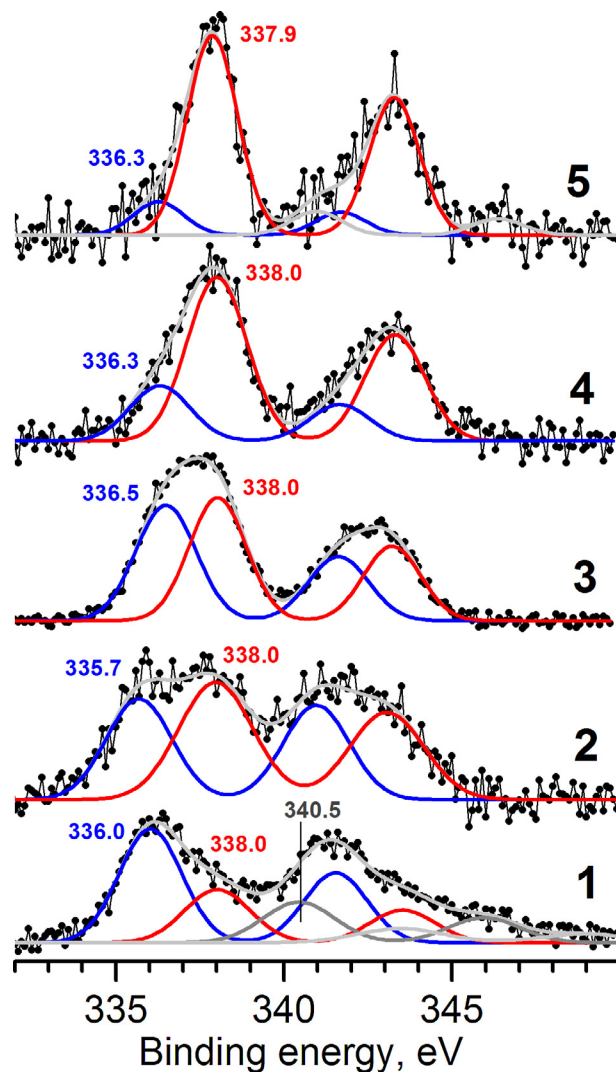

Fig. 6. Pd3d spectra of the 3PdCe-BR (1), 3PdCe-AR (2), 3PdCe-600-BR (3), 3PdCe-700-BR (4), and 3PdCe-800-BR (5) samples.

of palladium. The appearance of this component may be explained by relaxation shake-up effects related to Pd–C, which are caused by the composite structure. Because Pd particles are included in the carbon matrix, in which carbon is mainly in the sp^2 hybrid state, some of the electrons emitted from the 3d level of the palladium atoms, which is close in energy to the C1s level, can induce π–π^* transitions in the carbon atoms composing the graphite matrix that supports the palladium particles. The electron energy loss may produce intense satellites concurrent with a positive shift in the binding energy with respect to the ground state. In this case, the shift is 4.5 eV, which is close to the values of the shake-up effects in π-system of sp^2 structures (Fig. 5a, curves 1–3).

Table 2
Surface compositions of the samples versus calcination temperature.

Sample	Surface composition						
	C	O	Ce	Pd	C/Ce	Pd(336)/Pd(338)	Ce^{3+}/Ce
3PdCe-BR	85	12	3.4	0.10	25.1	1.79	65
3PdCe-AR	84	13	2.3	0.12	36.5	0.84	44
3PdCe-600	57	29	13.9	0.44	4.1	0.96	32
3PdCe-700	42	41	16.2	0.72	2.6	0.34	28
3PdCe-800	32	47	20.6	1.26	1.5	0.17	20
3.8Pd/CeO$_2$-P-700	16	53	29	1.3	0.6	0.5	23

Therefore, the XPS data are in full agreement with the HRTEM and XRD data, which indicate the presence of palladium carbide nanoparticles occluded in the graphite matrix. A smaller portion of palladium is in the oxidized state and interacts with cerium oxide (E_b(Pd3d$_{5/2}$) = 338.0 eV).

The treatment of the composite with the oxidative reaction medium increases the intensity of the component having the binding energy of 338.0 eV (Fig. 6, curve 2), which is characteristic of the formation of ionic palladium species and their dissolution in a cerium oxide lattice. However, the intensity of the main component decreases and experiences a small shift to 335.7 eV. The peak for the electron energy losses at 340.5 eV disappears, indicating the removal of the carbon layers from the surface of the palladium. This spectral behavior corresponds to carbon elimination from the composite and a partial transition of palladium from the carbide-like state to the metallic one.

Calcination of the composite at 600 °C results in a considerable growth in the total intensity of the Pd3d line (Table 2), which is related to the removal of carbon from the composite matrix. In addition to the total intensity growth of the Pd3d line, a shift of the low-energy component to 336.5 eV is observed (Fig. 6.3), which corresponds to the appearance of oxidized palladium clusters and PdO nanoparticles [46]. Therefore, treatment in oxygen at 600 °C leads to a complete transition of palladium from the carbide-like to the oxidized state and produces two oxide species: PdO nanoparticles and PdCeO$_x$ mixed oxide particles.

An increase in the calcination temperature to 700 °C leads to further interaction of the palladium with cerium oxide, as well as to the transition of the PdO phase to the PdCeO$_x$ mixed oxide phase, which can be deduced from the decrease in the intensity of the component at 336.4 eV (Fig. 6.4) and the increase in the intensity of the component at 338.0 eV.

The further elevation of the calcination temperature results in the enhancement of this effect. Palladium dissolves almost completely in the cerium oxide lattice to form the Pd$_x$Ce$_{1-x}$O$_2$ solid solution. This phenomenon is indicated by the presence of a single narrow component with a binding energy of 337.9 eV in the Pd3d spectrum of this catalyst (Fig. 6.5). The intensity of the additional state at 336.3 eV is quite low. Additionally, the XRD data indicates the formation of a small amount of PdO phase in this sample. The absence of PdO components with BE = 337.0 eV in this spectrum can be related to the rather large size of the PdO particles, which result in the minimal contribution of this signal to the integral spectrum.

It should be noted that the presence of 32 at.% carbon on the surface of composite calcined at 800 °C, according to XPS data, is not related to the presence of extended carbon structures. The presence of carbon on the surface of catalysts obtained by preparative chemical methods is a typical phenomenon. Table 2 shows the surface composition of the reference catalyst 3.8Pd/CeO$_2$-P-700, which has 16% carbon on its surface. The absence of extended carbon structures in the composite calcined at 800 °C is confirmed by such bulk-sensitive methods as XRD and Raman spectroscopy. This carbon can be present as low-molecular weight compounds on the surface, domain boundaries and other defects. It cannot be ruled out that this carbon can also stabilize surface defects of the catalyst and thus hinders sintering of the phase at elevated calcination temperatures.

The initial composite consists of strongly carbonized palladium and cerium particles, which are virtually encapsulated in the carbon matrix. Calcination in oxygen leads to the gradual elimination of carbon and the dissolution of palladium in cerium oxide. These events strongly enhance the catalytic activity.

Pd3d spectra obtained for composite calcined at 700 °C and reference catalyst 3.8Pd/CeO2-P-700 are shown on Fig. 6. The state of palladium on the surface of reference catalyst 3.8Pd/CeO2-P-700 (Fig. 7b) is also represented by two species: the solid solution
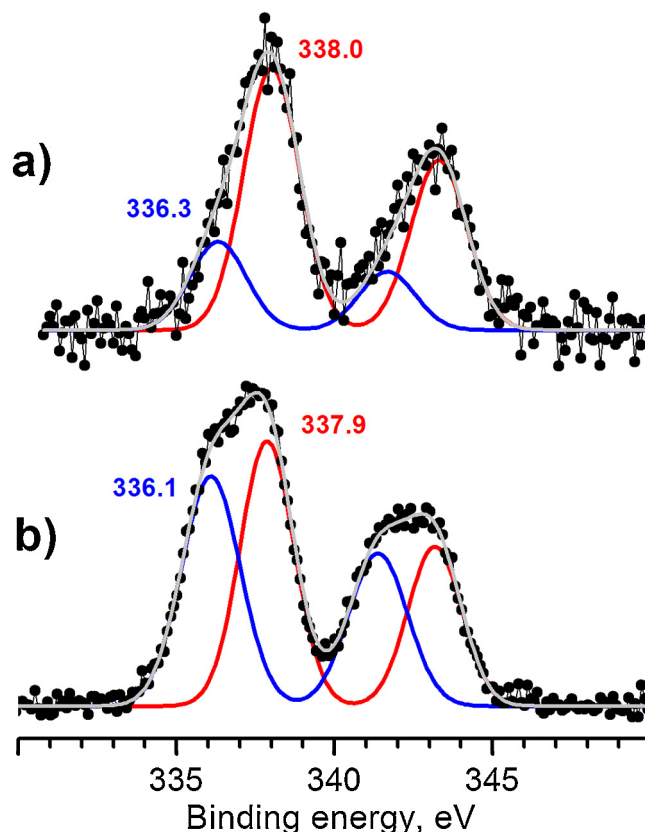

Fig. 7. Pd3d spectra of line for 3PdCeC-700 (a) and 3.8Pd/CeO2-P-700 (b) samples.

(E_b Pd3d$_{5/2}$ = 337.9 eV) and the oxidized palladium clusters (E_b Pd3d$_{5/2}$ = 336.1 eV). It means that a set of palladium states in the reference catalyst is similar to that in 3PdCeC-700; the only distinction is that the fraction of the state corresponding to surface palladium oxide clusters is lower in the latter case. Nevertheless, it should be noted that the spectra have no peaks typical of bulk metallic palladium (E_b Pd3d$_{5/2}$ = 336.9 eV) and PdO oxide (E_b Pd3d$_{5/2}$ = 336.9 eV), which are inactive in the LTO CO range. The presence of PdO phase recorded by XRD is not detected in the XPS spectra, probably due to a low amount of PdO particles and their relatively large size. Thus, palladium may be present mainly in the composition of two species, which are characterized by two states with E_b Pd3d$_{5/2}$ ∼ 336 eV and 338 eV.

3.5. Raman spectroscopy data

The Raman spectra for the samples of the 3PdCe composite calcined at 600, 700 and 800 °C are depicted in Fig. 8. These spectra are typical of the defect structure of CeO$_2$. According to [33,58–60], the main peak at 460 cm^{-1} corresponds to the F$_{2g}$ mode of the CeO$_2$ fluorine lattice. The band at 1160 cm^{-1} is attributed to the second order longitudinal optical mode (2LO), the bands in the range of 550–600 cm^{-1} correspond to the so-called defect-induced mode (D-mode), and the band at 250 cm^{-1} (a low peak) is the second order transverse acoustic mode (2TA). According to the authors of [61], the intensity of the shoulder near 570 cm^{-1}, with respect to the intensity of the main line near 460 cm^{-1}, may be related to oxygen vacancies and cation-doped inclusions.

Moreover, the shift of the F$_{2g}$ mode decreases from 454 to 445 cm^{-1} with increasing calcination temperature from 600 to 700 °C; on the contrary, a further increase of calcination temperature to 800 °C increases the band shift to 452 cm^{-1}. The shift of this band is caused by both the small size of the sample particles
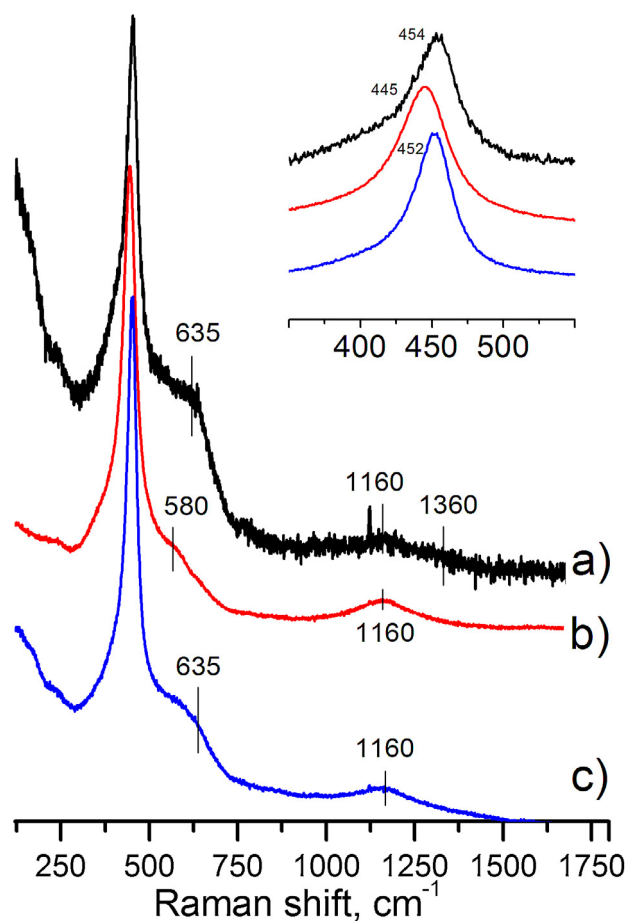
Fig. 8. Raman spectra of the 3PdCeC-600-BR, 3PdCeC-700-BR and 3PdCeC-800-BR samples.

and the high extent of their structural defects [58,59]. In addition, the authors of [18] observed a linear decrease in the Raman shift of the F_{2g} mode from 464 to 453 cm^{-1} with increasing the fraction of palladium in $Pd_xCe_{1-x}O_{2-\delta}$ solid solutions from $x = 0$ to $x = 0.18$. Thus, such behavior of the Raman spectra at increasing calcination temperature may point to several effects: dissolution of palladium oxide in cerium oxide to form a solid solution (a decrease in the Raman shift of the F_{2g} mode), annealing of the defects, sintering of the particles and decomposition of the solid solution at high calcination temperatures (a decrease in the Raman shift of the F_{2g} mode).

As seen in Fig. 8 the width of the main band of the F_{2g} mode decreases with increasing calcination temperature of the composite. The narrowing of the line results from an increase in the size of the cerium oxide crystallites [58,59]. However the intensity of the D-mode at 580 cm^{-1} remains very high in all cases, indicating the conservation of the high concentration of defects in the fluorite structure.

Notably, there are no bands at 1360 cm^{-1} (D-band) and 1580–1620 cm^{-1} (G-band), which are typical of carbon, observed in the spectra [62,63]. A trace of the D-band can be assumed only in the case of the 3PdCe-600-BR sample (Fig. 8a). These data indicate the absence of bulk carbon structures in the samples.

In addition to the bands corresponding to the defect structure of cerium oxide, a band typical of palladium oxide is observed at 635 cm^{-1}, which corresponds to the B_{1g} mode of square planar [PdO$_4$] subunits in the structure of palladium oxide [64]. In the spectrum obtained for the 3PdCeC-600-BR sample, this component shows up as a shoulder. When the calcination temperature

is increased to 700 °C, this shoulder nearly vanishes; this signal appears again in the 3PdCeC-800-BR sample when the calcination temperature is increased to 800 °C. The disappearance of this shoulder in the 3PdCeC-700-BR sample can be attributed to the dissolution of palladium oxide clusters initially present in the cerium oxide matrix when the $Pd_xCe_{1-x}O_2$ solid solution forms. These results are validated by the XPS data for the 3PdCeC-600-BR and 3PdCeC-700-BR samples (Fig. 6.3 and 6.4). The reappearance of this shoulder after the continued elevation of the calcination temperature can be ascribed to the decomposition of the $Pd_xCe_{1-x}O_2$ solid solution into individual cerium and palladium oxides. This result validates the XRD data for these samples (Fig. 1, curve d). Therefore, 700 °C is the optimal calcination temperature for these nanocomposites because the initial oxides blend almost completely forms a stable joint solid solution.

3.6. Features of the plasma-arc synthesis of Pd/CeO$_2$ catalysts

The two-step plasma-arc synthesis of the $Pd_xCe_{1-x}O_2$ composite catalysts demonstrates high catalytic performance in the low-temperature oxidation of CO. The proposed method of synthesis is simple to implement and is not time-consuming; it solves several problems related to the development of an active catalyst for the low-temperature oxidation of CO. First, these catalysts possess a high specific surface area, which does not shrink at temperatures up to 800 °C, i.e., the catalyst nanoparticles have a high concentration of active sites, and, because they also have high sintering resistance, the number of such sites remains quite large up to a temperature of 800 °C. Second, the synthesis conditions provide a uniform distribution of palladium over the entire cerium oxide lattice in the synthesized and calcined composite. This high dispersion leads to the formation of $Pd_xCe_{1-x}O_2$ solid solutions with a high defect structure and a substantial concentration of both anionic vacancies and Ce^{3+} ions.

In a series of papers by Machida and coworkers [34,37] the arc-plasma processing was used to produce Pd, Pt, Rh supported catalysts. Their technique allowed the authors to synthesize for CO oxidation the highly active Pd, Pt ceria based catalysts [36,37]. Machida's technique is more complicated because it is based on the vacuum deposition of metallic nanoparticles on the presynthesized powder of support (Al$_2$O$_3$, CeO$_2$ and AlPO$_4$) with subsequent catalyst activation by the high temperature treatment at 900 °C in O$_2$/H$_2$O mixture. In the method proposed by us it is not required such high temperature treatment, and the formation of finely dispersed support and the catalyst activation occurs simultaneously.

A comprehensive study using physical methods allowed us to reveal the key role of carbon in the formation of these palladium–cerium catalysts. The key components of the initial state of the catalyst are metallic; these components are highly dispersed palladium and cerium particles accumulated in carbon structures, with palladium covered in a carbide film that inhibits catalytic activity. As was shown in our earlier work [65], carbon structures obtained by plasma-arc synthesis are characterized by the formation of a variety of species with different dispersions. The simultaneous sputtering of all the components enables the production of the PdCeC composite material, which has palladium, cerium and carbon occurring as thoroughly distributed nanoparticles. This material can be transformed into a highly active catalyst by calcination in oxygen, which eliminates carbon and converts the composite components to an oxidized form. In the process, highly dispersed metallic palladium makes contact with cerium and the chemical reaction to produce a $Pd_xCe_{1-x}O_2$ solution, which is the catalytically active phase for the low-temperature oxidation of CO. Analysis of the XPS spectra showed that the calcination of the PdCeC composite leads primarily to the elimination of amorphous
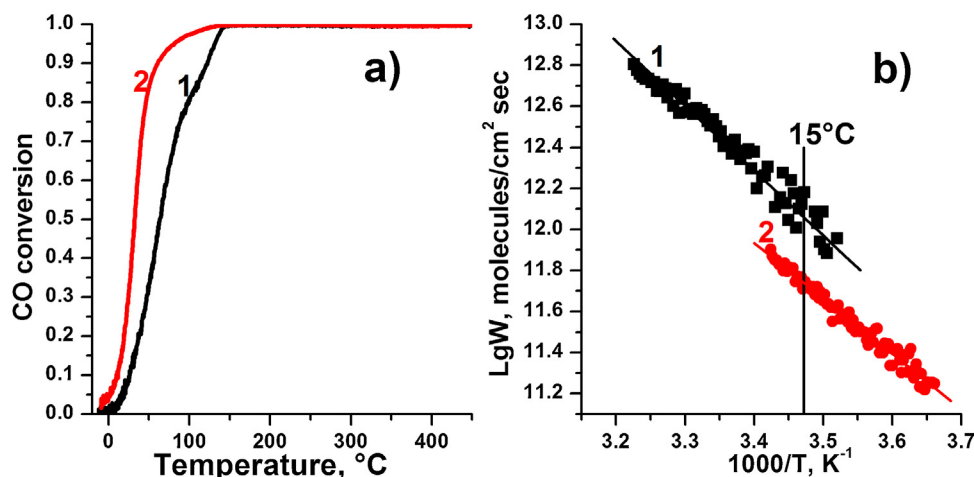
Fig. 9. (a) Temperature dependences of CO conversion, and (b) Arrhenius dependences of CO oxidation rate for catalysts 3PdCe-700 (1) and 3.8Pd/CeO$_2$-P-700 (2).

carbon and sp^2 hybridized carbon structures. However, even when the calcination temperature is as high as 800 °C, the catalyst structure retains residual incombustible carbon in the sp^3 hybridized state. According to Raman spectroscopy, the catalyst samples synthesized using the proposed technique have numerous structural defects. The XPS and Raman spectroscopy data suggest that the sp^3 carbons located in the Pd$_x$Ce$_{1-x}$O$_2$ structure are responsible for the distortion of the lattice and the stabilization of the defects.

Interestingly, all catalysts obtained by incipient wetness impregnation (IWI), coprecipitation or other chemical methods [15,16,44–46], which were examined by XPS in our earlier works, always retained a large amount of carbon on the surface. The high reactivity of the defect surface of the cerium oxide nanoparticles probably allows this carbon to be deposited during the synthesis of the catalyst. Efficient carbonization of ceria-based catalysts via the action of hydrocarbons or carbon oxides has also been reported in the literature [66–68]. These results suggest that the carbon admixture in the cerium oxide moiety may play an essential role in the generation and stabilization of its defect structure, and carbon, because it has a small atomic radius, tends to occupy vacancies in the structural defects primarily in the surface-subsurface layers. These literature data strongly corroborate our conclusions concerning the role of sp^2 and sp^3 carbon structures in the initial composite. To initiate catalytic activity, excessive carbon must be eliminated. However, to provide stable operation of the catalysts over a wide temperature range, a certain amount of nonreactive sp^3 carbon must remain in the lattice defects of the palladium–cerium catalyst.

3.7. Comparison with catalysts prepared by conventional impregnation techniques

This paper deals with the synthesis of catalytically active materials obtained by a physical, rather than chemical, method. Therefore, we were interested in the comparison of the catalytic activity of the synthesized samples with the activity of those prepared by standard chemical methods.

A catalyst prepared by the coprecipitation method with nearly the same palladium content 3.8Pd/CeO$_2$-P-700 was tested against the 3PdCe-700 sample. The chosen catalysts were calcined at the same temperature and also possessed similar values for specific surface area (66 m^2/g). Both catalysts had a fluorite structure composed of cerium oxide and an extremely high dispersion of palladium. The EDX method revealed the presence of palladium even in regions where palladium structures are undetectable by HRTEM. This observation implies the existence of an extremely high

dispersion of palladium up to the formation of the Pd$_x$Ce$_{1-x}$O$_2$ solid solutions.

A comparison of the temperature effects on conversion for the indicated catalysts is illustrated in Fig. 9a. As seen from the figure, the increase of CO conversion for the 3.8Pd/CeO$_2$-P-700 (curve 1) catalyst occurs at lower temperatures than for 3PdCe-700 sample (curve 2). The ignition temperature (T_{10}) is 10 °C and 25 °C for 3.8Pd/CeO$_2$-P-700 and for 3PdCe-700 samples, respectively. Also, the 3PdCe-700 catalyst is characterized by a higher T_{50} value, 65 °C, compared with the 3.8Pd/CeO$_2$-P-700 sample, for which T_{50} is equal to 30 °C. However, for precise comparison of catalytic activity we need to take into account the dispersion of active component and the sample weight in reactor. In the case of Pd/CeO$_2$ catalysts there is maximal dispersion, so it is necessary to use the same weight of active component in reactor. Unfortunately, the catalysts obtained by the chemical and the plasma-arc methods had a different apparent density (0.176 and 0.696 g/cm^3 for 3PdCe-700 and 3.8Pd/CeO$_2$-P-700 samples, respectively), while the volume of the sample in the reactor was constant, so the catalyst weight, and the amount of the active component, too, for the samples being compared were different. Ultimately, it is difficult to ascertain which of the catalysts is more active in the CO + O$_2$ reaction, if we analyze the CO conversion curves only.

To compare the specific catalytic activities, we calculated for both catalysts the rates of CO oxidation at 5–20% conversions and turnover frequencies (TOFs) referred to entire palladium present in the catalyst. Reaction rate was calculated using the formula: W (molecules/cm^2 s) $= (C_{CO}^0 \times X \times V_{RM})/(m \times S_{sp})$, where C_{CO}^0 is the initial concentration of CO (molecules/cm^3), X is the CO conversion, V_{RM} is the reaction mixture flow rate (cm^3/s), m is the catalyst weight (g), S_{sp} is the specific surface area (cm^2/g). Fig. 9b displays the Arrhenius dependences of the CO oxidation rate for 3PdCe-700 and 3.8Pd/CeO$_2$-P-700. The calculated activation energies are equal to 14.5 and 12.4 kcal/mol for 3PdCe-700 and 3.8Pd/CeO$_2$-P-700 samples, respectively. TOFs were calculated using the formula TOF = W (molecules/cm^2 sec)/Pd (atom Pd/cm^2) at a temperature of 15 °C.

The state of palladium on the surface of PdCeC-700 composite does not differ from that in 3.8Pd/CeO$_2$-P-700 catalyst and is represented by the solid solution with E_b Pd3d$_{5/2}$ = 337.9–338.0 eV and the oxidized surface clusters of PdO$_x$ with E_b Pd3d$_{5/2}$ = 336.1–336.3 eV. According to XPS data, the PdO oxide and the metal are absent on the surface in both cases. Thus, the total chemical state of palladium on the surface of these catalysts can be considered as atomically dispersed; to a first

approximation, the entire palladium on the surface is accessible to the reaction medium. Moreover, we showed earlier that a state with the binding energy 336.1 eV is also directly involved in the catalytic reaction $CO + O_2$ at low temperatures [46]. Taking into account the comparable values of specific surface area (66 m^2/g for PdCeC-700 and 38 m^2/g for 3.8Pd/CeO$_2$-P-700) and close concentrations of palladium, we decided it would be correct to compare the catalysts using the TOF values referred to the entire palladium introduced into the catalyst. However, it seems difficult to reveal an exact ratio of accessible palladium on the surface to that in the bulk. Nevertheless, such method of normalizing the catalytic activity is now the most reasonable and optimal one.

The obtained values are 4.5 and 1.7 s^{-1} for the 3PdCe-700 and the 3.8Pd/CeO$_2$-P-700 catalysts, respectively. Therefore, the TOF value of 3PdCe-700 is about 2.5 times higher than that of the 3.8Pd/CeO$_2$-P-700 sample. Thus, the precise comparison of two Pd/CeO$_2$ catalysts, prepared by plasma-arc and coprecipitation methods and characterized by similar composition and surface specific areas, allows us make reliable conclusion on the possibility to apply plasma-arc synthesis for highly active Pd/CeO$_2$ catalysts for low-temperature CO oxidation.

4. Conclusions

The plasma-arc method was applied to synthesize composite palladium–cerium catalysts for the low-temperature oxidation of carbon monoxide. The synthesis of Pd/CeO$_2$ catalysts was carried out in two steps: step 1 – direct synthesis of the PdCeC composite in the plasma-arc chamber, and step 2 – calcination of the composite in air at 600, 700, and 800 °C. The synthesized catalysts are highly efficient toward the oxidation of carbon monoxide and are able to oxidize CO at temperatures as low as room temperature. Physical methods (HRTEM, XRD, XPS, Raman spectroscopy and others) were used to comprehensively investigate the microstructure, composition and electronic state of the composite components after the high-temperature calcination step. The high catalytic activity is facilitated by the formation of a high-defect fluorite structure a solid solution PdCeO$_x$ and highly dispersed PdO$_x$ nanoparticles. The XPS data suggest that the carbon nanostructures, which are mixed with palladium and cerium in the initial PdCeC composite, play a key role in the formation of the high-defect solid solution of palladium in the CeO$_2$ structure. We also think that carbon clusters incorporated into the catalyst structure prevent dramatic sintering during high-temperature calcination and provide a highly dispersed state in the catalyst.

A comparison with a catalyst prepared by coprecipitation that had similar morphology and palladium content showed a two–three fold greater TOF value for the catalyst prepared by the plasma-arc method.

Acknowledgments

Appendix A. Supplementary data

Supplementary data associated with this article can be found, in the online version, at http://dx.doi.org/10.1016/j.apcatb.2013.08.043.

References

[1] P. Euzen, J.-H. Le Gal, B. Rebours, G. Martin, Catalysis Today 47 (1999) 19–27.
[2] K.-i. Fujimoto, F.H. Ribeiro, M. Avalos-Borja, E. Iglesia, Journal of Catalysis 179 (1998) 431–442.
[3] P.O. Thevenin, A. Alcalde, L.J. Pettersson, S.G. Järås, J.L.G. Fierro, Journal of Catalysis 215 (2003) 78–86.
[4] L.-H. Xiao, K.-P. Sun, X.-L. Xu, X.-N. Li, Catalysis Communications 6 (2005) 796–801.
[5] J.-Y. Luo, M. Meng, J.-S. Yao, X.-G. Li, Y.-Q. Zha, X. Wang, T.-Y. Zhang, Applied Catalysis B: Environmental 87 (2009) 92–103.
[6] S. Colussi, A. Gayen, M. Farnesi|Camellone, M. Boaro, J. Llorca, S. Fabris, A. Trovarelli, Angewandte Chemie International Edition 48 (2009) 8481–8484.
[7] K.R. Priolkar, P. Bera, P.R. Sarode, M.S. Hegde, S. Emura, R. Kumashiro, N.P. Lalla, Chemistry of Materials 14 (2002) 2120–2128.
[8] P. Bera, K.C. Patil, V. Jayaram, G.N. Subbanna, M.S. Hegde, Journal of Catalysis 196 (2000) 293–301.
[9] G. Glaspell, H. Hassan, A. Elzatahry, V. Abdalsayed, M. El-Shall, Topics in Catalysis 47 (2008) 22–31.
[10] S. Royer, D. Duprez, ChemCatChem 3 (2011) 24–65.
[11] M.S. Hegde, G. Madras, K.C. Patil, Accounts of Chemical Research 42 (2009) 704–712.
[12] A. Trovarelli, Catalysis Reviews – Science and Engineering 38 (1996) 439–520.
[13] H. He, H.X. Dai, C.T. Au, Catalysis Today 90 (2004) 245–254.
[14] G. Li, Q. Wang, B. Zhao, R. Zhou, Catalysis Today 158 (2010) 385–392.
[15] A.I. Boronin, E.M. Slavinskaya, I.G. Danilova, R.V. Gulyaev, Y.I. Amosov, P.A. Kuznetsov, I.A. Polukhina, S.V. Koscheev, V.I. Zaikovskii, A.S. Noskov, Catalysis Today 144 (2009) 201–211.
[16] A.S. Ivanova, E.M. Slavinskaya, R.V. Gulyaev, V.I. Zaikovskii, O.A. Stonkus, I.G. Danilova, L.M. Plyasova, I.A. Polukhina, A.I. Boronin, Applied Catalysis B: Environmental 97 (2010) 57–71.
[17] T. Baidya, G. Dutta, M.S. Hegde, U.V. Waghmare, Dalton Transactions (2009) 455–464.
[18] M. Kurnatowska, L. Kepinski, W. Mista, Applied Catalysis B: Environmental 117–118 (2012) 135–147.
[19] S. Roy, M.S. Hegde, N. Ravishankar, G. Madras, Journal of Physical Chemistry C 111 (2007) 8153–8160.
[20] A.D. Mayernick, M.J. Janik, Journal of Physical Chemistry C Nanomaterials and Interfaces 112 (2008) 14955–14964.
[21] A.D. Mayernick, M.J. Janik, Journal of Chemical Physics 131 (2009) 084701–084712.
[22] Z. Yang, Z. Lu, G. Luo, K. Hermansson, Physics Letters A 369 (2007) 132–139.
[23] Z. Yang, G. Luo, Z. Lu, K. Hermansson, Journal of Chemical Physics 127 (2007) 074704–074705.
[24] M. Nolan, Journal of Materials Chemistry 21 (2011) 9160–9168.
[25] D.O. Scanlon, B.J. Morgan, G.W. Watson, Physical Chemistry Chemical Physics 13 (2011) 4279–4284.
[26] H. Zhu, Z. Qin, W. Shan, W. Shen, J. Wang, Journal of Catalysis 233 (2005) 41–50.
[27] R. Craciun, W. Daniell, H. Knözinger, Applied Catalysis A: General 230 (2002) 153–168.
[28] F. Bozon-Verduraz, A. Omar, J. Escard, B. Pontvianne, Journal of Catalysis 53 (1978) 126–134.
[29] W.-J. Shen, Y. Matsumura, Journal of Molecular Catalysis A: Chemical 153 (2000) 165–168.
[30] M. Cargnello, T. Montini, S. Polizzi, N.L. Wieder, R.J. Gorte, M. Graziani, P. Fornasiero, Dalton Transactions 39 (2010) 2122–2127.
[31] R. Strobel, A. Alfons, S.E. Pratsinis, Advanced Powder Technology 17 (2006) 457–480.
[32] K. Zhou, X. Wang, X. Sun, Q. Peng, Y. Li, Journal of Catalysis 229 (2005) 206–212.
[33] Z. Wu, M. Li, J. Howe, H.M. Meyer, S.H. Overbury, Langmuir 26 (2010) 16595–16606.
[34] S. Hinokuma, K. Murakami, K. Uemura, M. Matsuda, K. Ikeue, N. Tsukahara, M. MacHida, Topics in Catalysis 52 (2009) 2108–2111.
[35] S. Hinokuma, M. Okamoto, E. Ando, K. Ikeue, M. MacHida, Catalysis Today 175 (2011) 593–597.
[36] S. Hinokuma, M. Okamoto, E. Ando, K. Ikeue, M. MacHida, Bulletin of the Chemical Society of Japan 85 (2012) 144–149.
[37] S. Hinokuma, Y. Katsuhara, E. Ando, K. Ikeue, M. Machida, Catalysis Today 201 (2013) 92–97.
[38] W. Kratschmer, L.D. Lamb, K. Fostiropoulos, D.R. Huffman, Nature 347 (1990) 354–358.
[39] S. Iijima, Nature 354 (1991) 56–58.
[40] V.A. Maltsev, O.A. Nerushev, S.A. Novopashin, S.Z. Sakhapov, D.V. Smovzh, Russian Nanotechnology 2 (2007) 85–89.
[41] J.H.J. Scott, S.A. Majetich, Physical Review B 52 (1995) 12564–12571.
[42] E. Slavinskaya, R. Gulyaev, O. Stonkus, A. Zadesenets, P. Plyusnin, Y. Shubin, S. Korenev, A. Ivanova, V. Zaikovskii, I. Danilova, A. Boronin, Kinetics and Catalysis 52 (2011) 282–295.
[43] P. Scherrer, Gottinger Nachrichten 2 (1918) 98–103.
[44] J.F. Moulder, W.F. Strickle, P.E. Sobol, K.D. Bomben, in: Chastain J. (Ed.), A reference book of standart spectra for identification and interpretation of XPS data, Perkin-Elmer Corporation Physical Electronics Division, USA, 1992.
[45] E.M. Slavinskaya, O.A. Stonkus, R.V. Gulyaev, A.S. Ivanova, V.I. Zaikovskii, P.A. Kuznetsov, A.I. Boronin, Applied Catalysis A: General 401 (2011) 83–97.
[46] R.V. Gulyaev, A.I. Stadnichenko, E.M. Slavinskaya, A.S. Ivanova, S.V. Koscheev, A.I. Boronin, Applied Catalysis A: General 439–440 (2012) 41–50.
[47] P. Singh, M.S. Hegde, Crystal Growth and Design 10 (2010) 2995–3004.
[48] B. Wang, D. Weng, X. Wu, R. Ran, Applied Surface Science 257 (2011) 3878–3883.

[49] Y. Luo, Y. Xiao, G. Cai, Y. Zheng, K. Wei, Applied Catalysis B: Environmental 136–137 (2013) 317–324.

[50] L.M. Misch, J.A. Kurzman, A.R. Derk, Y.-I. Kim, R. Seshadri, H. Metiu, E.W. McFarland, G.D. Stucky, Chemistry of Materials 23 (2011) 5432–5439.

[51] A.P. Dementjev, K.I. Maslakov, Applied Surface Science 253 (2006) 1095–1100.

[52] A.P. Dementjev, K.I. Maslakov, A.V. Naumkin, Applied Surface Science 245 (2005) 128–134.

[53] S.-H. Oh, G.B. Hoflund, Journal of Catalysis 245 (2007) 35–44.

[54] H. Gabasch, W. Unterberger, K. Hayek, B. Klötzer, E. Kleimenov, D. Teschner, S. Zafeiratos, M. Hävecker, A. Knop-Gericke, R. Schlögl, J. Han, F.H. Ribeiro, B. Aszalos-Kiss, T. Curtin, D. Zemlyanov, Surface Science 600 (2006) 2980–2989.

[55] M.G. Mason, Physical Review B 27 (1983) 748–762.

[56] G.K. Wertheim, Zeitschrift für Physik D Atoms, Molecules and Clusters 12 (1989) 319–326.

[57] R. Westerström, M.E. Messing, S. Blomberg, A. Hellman, H. Grönbeck, J. Gustafson, N.M. Martin, O. Balmes, R. Van Rijn, J.N. Andersen, K. Deppert, H. Bluhm, Z. Liu, M.E. Grass, M. Hävecker, E. Lundgren, Physical Review B – Condensed Matter and Materials Physics 83 (2011) 115440.

[58] W.H. Weber, K.C. Hass, J.R. McBride, Physical Review B 48 (1993) 178–185.

[59] I. Kosacki, T. Suzuki, H.U. Anderson, P. Colomban, Solid State Ionics 149 (2002) 99–105.

[60] M. Daniel, S. Loridant, Journal of Raman Spectroscopy 43 (2012) 1312–1319.

[61] Y. Lee, G. He, A.J. Akey, R. Si, M. Flytzani-Stephanopoulos, I.P. Herman, Journal of the American Chemical Society 133 (2011) 12952–12955.

[62] A.C. Ferrari, Diamond and Related Materials 11 (2002) 1053–1061.

[63] M. Kawakami, H. Kanba, K. Sato, T. Takenaka, S. Gupta, R. Chandratilleke, V. Sahajwalla, ISIJ International 46 (2006) 1165–1170.

[64] J.R. McBride, K.C. Hass, W.H. Weber, Physical Review B 44 (1991) 5016–5028.

[65] A.E. Belikov, A.V. Zaikovskii, V.A. Maltsev, O.A. Nerushev, S.A. Novopashin, V.P. Paharukova, P.V. Snytnikov, S.Z. Sakhapov, D.V. Smovzh, Thermophysics and Aeromechanics 16 (2009) 691–694.

[66] M. Swanson, V.V. Pushkarev, V.I. Kovalchuk, J.L. D'Itri, Catalysis Letters 116 (2007) 41–45.

[67] C. Li, Y. Sakata, T. Arai, K. Domen, K. Maruya, T. Onishi, Journal of the Chemical Society: Chemical Communications 0 (1991) 410–411.

[68] M.E. Swanson, V.V. Pushkarev, V.I. Kovalchuk, J.L. d'Itri, Journal of Siberian Federal University. Chemistry 3 (2010) 207–215.